COMMUNICATION

Boron Nitride

NANO · MICRO

small
www.small-journal.com

Check for updates

Hexagonal Boron Nitride Growth on Cu-Si Alloy: Morphologies and Large Domains

Jidong Li, Zhili Hu, Yangfan Yi, Maolin Yu, Xuemei Li, Jianxin Zhou, Jun Yin, Shiwei Wu, and Wanlin Guo*

Controllable synthesis of high-quality hexagonal boron nitride (h-BN) is desired toward the industrial application of 2D devices based on van der Waals heterostructures. Substantial efforts are devoted to synthesize h-BN on copper through chemical vapor deposition, which has been successfully applied to grow graphene. However, the progress in synthesizing h-BN has been significantly retarded, and it is still challenging to realize millimeter-scale domains and control their morphologies reliably. Here, the nucleation density of h-BN on Cu is successfully reduced by over two orders of magnitude by simply introducing a small amount of silicon, giving rise to large triangular domains with maximum 0.25 mm lateral size. Moreover, the domain morphologies can be modified from needles, tree patterns, and leaf darts to triangles through controlling the growth temperature. The presence of silicon alters the growth mechanism from attachment-limited mode to diffusion-limited mode, leading to dendrite domains that are rarely observed on pure Cu. A phase-field model is utilized to reveal the growing dynamics regarding B-N diffusion, desorption, flux, and reactivity variables, and explain the morphology evolution. The work sheds lights on the h-BN growth toward large single crystals and morphology probabilities.

2D hexagonal boron nitride (h-BN) is well known as a perfect complementary material for graphene. They share similar honeycomb lattice and van der Waal structure but possess quite different properties. Hexagonal boron nitride is a wide gap semiconductor[1] of chemically inertness[2] and an atomic flat surface. Encapsulating other 2D materials to screen the substrate and ambient environment, h-BN is the key for the high-quality performance of various 2D devices.[3] In addition, it is promising to serve as thermal protective coatings and ultraviolet optics.[4]

J. Li, Dr. Z. Hu, M. Yu, Dr. X. Li, Dr. J. Zhou, Dr. J. Yin, Prof. W. Guo
State Key Laboratory of Mechanics and Control of Mechanical Structures
Key Laboratory of Intelligent Nano Materials and Devices of DoE
Institute of Nano Science
Nanjing University of Aeronautics and Astronautics
Nanjing 210016, China
E-mail: wlguo@nuaa.edu.cn
Y. Yi, Prof. S. Wu
State Key Laboratory of Surface Physics
Key Laboratory of Micro and Nano Photonic Structures (MOE)
Department of Physics
Fudan University
Shanghai 200433, China

However, its potential applications are significantly suppressed due to the lack of large-scale production of high-quality film. The lateral dimension of single h-BN domain could hardly grow up to 100 µm,[5] while single crystalline graphene has achieved millimeter-scale domain growth via multiple routes such as oxygen assistant and using Cu-Ni alloy substrate.[6] However, the introduction of oxygen does not promote the large h-BN domain growth as we previously revealed.[7] Although Cu-Ni alloys can decrease the nucleation density of h-BN, the corresponding maximum grain size is still limited to ≈100 µm.[8] As far as we know, the maximum h-BN domain sizes are in several hundreds of micrometers and can be achieved on Si-doped Fe substrates,[9] Ni (111) films[10] or in Cu enclosures.[11]

To achieve higher degree of control over the domain size, deeper insights into the growing dynamics are required. However, the morphology evolution which is highly relative to the growth dynamics is rarely observed in previous high temperature chemical vapor deposition (CVD). Most crystalline h-BN domains grown on Cu or Ni are triangles of preferred *N*-terminated edges.[12] Only regular polygons, such as truncated triangles or hexagons, can be realized via tuning the B to N ratio of the source.[13] Dendrites are rarely reported since h-BN domains favor straight edges of specific lattice orientations due to the strong anisotropy of its edge energy.

Here, we introduced a small amount of silicon into Cu substrate and realized reliable controllability over the morphologies and nucleation densities of deposited h-BN domains. Dendritic and fractal growth of h-BN, which is seldom observed on Cu substrate, emerge on Si-doped Cu substrate and can be delicately tuned through the deposition temperature. In particular, novel shuriken shapes are found in a large quantity at ≈1025 °C on Cu substrate doped with ≈2.8 at% Si. Increasing growth temperature to near melting point, triangles dominate the domain shapes, and their nucleation density dramatically decreases by two orders of magnitude leading to large domains with maximum lateral size around 0.25 mm. Some large domains contain large bilayer area of either AA' or AB stacking sequence, which can be distinguished by their second harmonic generation (SHG). Compared with the attachment-limited growth on pure Cu, the presence of silicon alters the

growth to diffusion-limited regime, giving rise to the abundant morphologies and large domain size. Our phase field simulation verifies that diffusion and desorption of B-N feedstock play critical roles on the morphology evolution when changing the growth temperature.

Low pressure CVD is employed to deposit h-BN using ammonia borane as solid precursor. Cu-Si alloy substrate is prepared through melting mixture of Si and Cu particles under hydrogen protection (see the Experimental Section). **Figure 1**a shows the binary phase diagram of the Cu-Si system.[14] We grew h-BN in the yellow colored region of the phase diagram, where a small amount of silicon can thoroughly dissolve in Cu and form a solid solution with face-centered cubic (FCC) phase. Surprisingly, merely ≈2.8 at% Si content could significantly change the growth dynamics of h-BN on Cu. At high growth temperature around 1035 °C, h-BN domains keep triangular shape as those grown on the pure Cu substrate in spite of a slightly dented edge (Figure 1b). However, as we decrease the growth temperature to 1025 °C, apparent notches occur at the edge centers of triangular domains and some of them could even develop into perfect shuriken shape as shown in Figure 1c and Figure S1 in the Supporting Information. Further lowering down the growth temperature, only tree patterns survive with wide brunches at 1015 °C (Figure 1d) and needle brunches at 1000 °C (Figure 1e). Obvious fractal growth happens here, which can further develop into higher fractal dimension if lower deposition temperature was adopted (Figure S2, Supporting Information). These above-mentioned morphologies are roughly of triple symmetry, which should be mainly regulated by the anisotropy of edge energy of h-BN.

To explore the influence of silicon on h-BN growth, we changed its doping content in Cu from 0 to 2.8 at%. The same deposition temperature of 1030 °C is employed for all the samples here. On Cu substrate slightly doped with 0.5 at% Si, h-BN domains of ≈10 µm triangles were grown as shown in **Figure 2**a. Similar scenario was observed on pure Cu as we reported previously.[12a,15] The influence of Si doping on the h-BN growth was ignorable here. As the Si content increases, concaved edges start to show at 1.4 at% (Figure S3, Supporting Information) and notches appears at 2.4 at% (Figure 2b), meanwhile
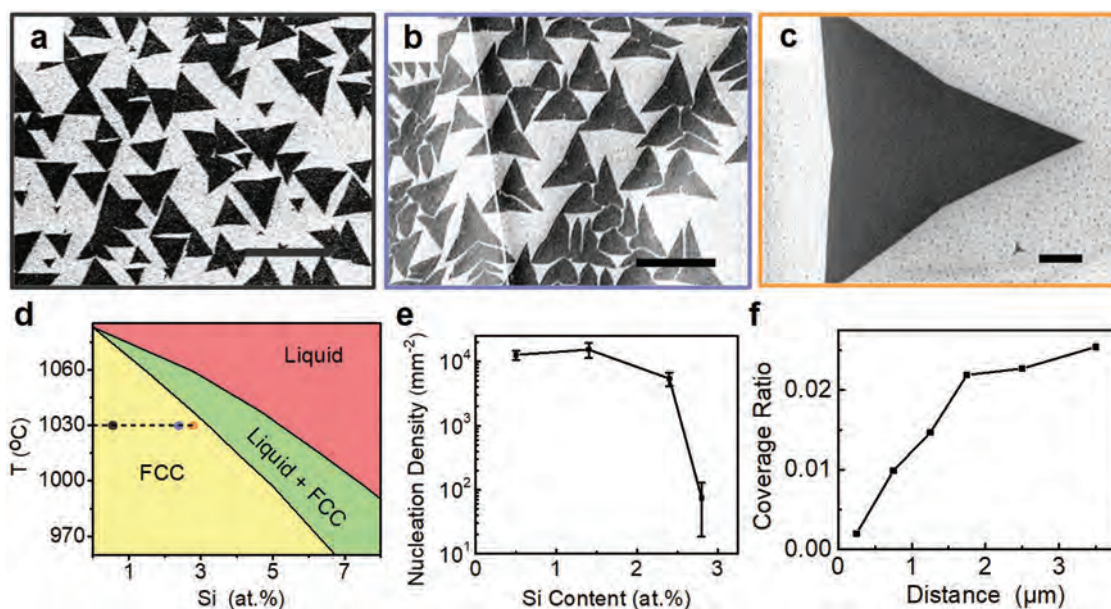
the melting point of substrate decreases. As illustrated in the phase diagram (Figure 2d), higher Si content would lead to lower melting point of Cu substrate. When the Si content reaches ≈2.8 at%, the substrate is quite close to the liquid phase at 1030 °C deposition temperature. Actually, the surface of alloy substrate does start melting as manifested by its wavy topography (Figure 1b). At this concentration of Si, the domain size is significantly increased and maximum ones we observed could reach ≈0.25 mm in lateral size (Figure S4, Supporting Information). We analyzed the dependence of nucleation density at 1030 °C on the Si concentration. As shown in Figure 2e, the nucleation density keeps almost constant until the Si content reaches ≈2.8 at%, where it dramatically decreases by two orders of magnitude. However, the high concentration of Si cannot be the only reason for the abrupt drop of nucleation density since the temperature also plays a critical role here. With the same ≈2.8 at% Si concentration but a growth temperature lower than 1025 °C, the nucleation density is obviously much larger than that at 1030 °C (Figure 1b–e). Only when the substrate almost starts to melt, large domains can appear, implying the phase transition of the substrate surface from solid to liquid can significantly suppresses the nucleation density.

Noticeably, although the nucleation density of clearly visible h-BN domain is quite low at 2.8 at% Si concentration and 1030 °C growth temperature, these large domains are always surrounded by plenty of tiny islands, as shown in Figure 2c. We calculated the average coverage ratio of these islands with respect to their normal distance from the large domain's edge and found that the closer these islands are to the large domain, the smaller coverage ratio they have (Figure 2f). The coverage area decreases by one order of magnitude at the distance ≈0.25 µm than that ≈3.5 µm. This growth pattern is fairly consistent with the Ostwald ripening, where large domains tend to consume the small islands as B-N source to grow up. These tiny islands are energetically unfavorable compared with large domains due to their high edge-surface ratio. Therefore, these islands prefer to be dissolved on the surface or into the substrate and provide B-N sources for their adjacent large domains.

During the CVD growth of h-BN on Cu, ammonia borane (H3BNH3), as the solid precursor in our CVD process,
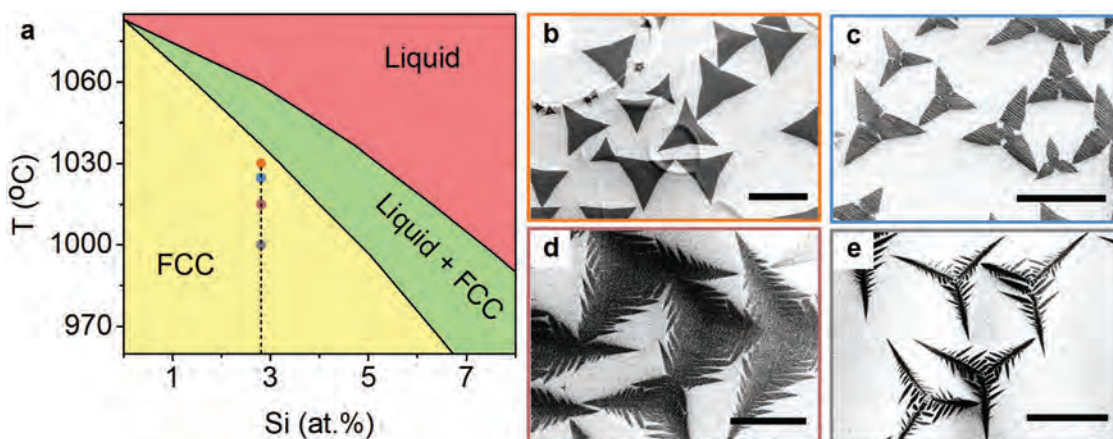
Figure 1. a) Phase diagram of the Cu-Si alloy with FCC phase highlighted by yellow, liquid phase by red, and mix phase by green color. b–e) Scanning electron microscope (SEM) images showing the domain morphologies grown at b) 1030, c) 1025, d) 1015, and e) 1000 °C, respectively, as marked by orange, blue, brown, and gray dots in panel (a), respectively. Scalar bars are 100 µm in panel (b) and 20 µm in panels (c–e).

ADVANCED
SCIENCE NEWS
www.advancedsciencenews.com

NANO · MICRO
small
www.small-journal.com

Figure 2. a–c) SEM images showing the domains grown on Cu substrate doped with a) ≈0.5, b) ≈2.4, and c) ≈2.8 at% Si. Scalar bars are 20 μm. d) Black, violet, and orange dots in phase diagram mark the corresponding growth condition for panels (a–c), respectively. e) Dependence of nucleation density on Si concentration in Cu substrate. f) Coverage area ratio of tiny nucleus adjacent to the large domain in panel (c) versus their normal distance to the nearest edge of the domain.

decomposed into volatile derivatives, mainly monomeric aminoborane (H2BNH2) in the temperature range we used.[16] Aminoborane flux was then carried into the growth chamber by hydrogen flow. The feedstock of aminoborane on substrate became balanced through their dynamic competition between adsorption and desorption. Cu surface catalyzed the dehydrogenation of aminoborane during its diffusion on the surface and thus produce B-N sources that can attach at the edges of the h-BN islands. However, the catalytic efficiency of Cu is slow and edges of h-BN domains are normally passivated by hydrogen atoms, lifting up the energy barrier for B-N attachment. Therefore, the attachment of B-N at the edge is generally limited due to the slow rate of dehydrogenation and incorporation. In this case, the edge energy dominates the morphologies. Nitrogen-terminated zigzag edges are energetically favored and that is the reason why most domains grown on Cu are equilateral triangles.[15] Increasing the ratio of B to N in the growth environments could favor B-terminated zigzag edges and thus vary the edge energy equilibrium.[17] Using this method, the morphologies can be tuned into polygons or curved polygons. Nevertheless, no dendrites occur with the attachment-limited growth. The dendritic and fractal growth is characteristic indication of the diffusion-limited growth, resulting from the interface instability.[18] Thus, silicon should play a critical role in transforming the edge-limited growth to the diffusion-limited growth on Cu.

Moreover, the experimental results also show that low growth temperature gives rise to sharp spine-like tips, while high growth temperature tends to bring about triangular tips on Si-doped Cu as shown in the first row of **Figure 3**. To reveal the underlying mechanism, we resorted to phase-field simulation.[19] The phase-field model is based on that of Srinivasan et al.[20] Several temperature-dependent parameters, including B-N diffusivity, deposition flux, desorption time, and attachment time, are examined to qualitatively understand their effect on the growth morphology and the results are shown in Figure 3 and Figure S5 in the Supporting Information. It indicates that less spiny shapes would evolve by either mildly increasing diffusivity/attachment time or decreasing flux/desorption time. However, several factors can be excluded as the dominance factors in our situation due to their inconsistency with experimental facts. For example, higher temperature would raise the chemical reactivity hence reduce the attachment time and cause spiny tips according to the simulation. It contradicts with the experiments where obtuse tips always appear with higher growth temperature. In addition, the flux is mainly determined by the heat treatment of the ammonia borane source from the upstream, which is nearly constant in all our experiments. So, the influence of growth temperature on the deposition flux could be neglected. On the other hand, at higher temperature, diffusion and desorption would be faster, causing less spiny crystal grain shapes, which agrees with the experiment. To this point, we conclude that the temperature-dependent diffusion/desorption dominated the morphology evolution. Noticeably, diffusion is also a dominant factor in the diffusion-limited growth on Si-doped Cu substrate. Considering the fast growth of single large domain on Si-doped substrate as shown in Figure 2c, the high growth speed suggests the edge attachment is accelerated by the silicon dopant, probably via dehydrogenation of the aminoborane or passivated edge, and thus brings the growth mode into diffusion-limited regime. Besides, silicon has been suggested to promote the dehydration of borazine on Cu and facilitate the catalytic growth of h-BN, providing more B-N source.[10] Here, we performed first-principle calculations on the dehydrogenation process as schematically illustrated in Figure S7 in the Supporting Information. With the assistant of Si, the energy consumed to remove the hydrogen from B-N-H

ADVANCED
SCIENCE NEWS
www.advancedsciencenews.com

NANO · MICRO
small
www.small-journal.com
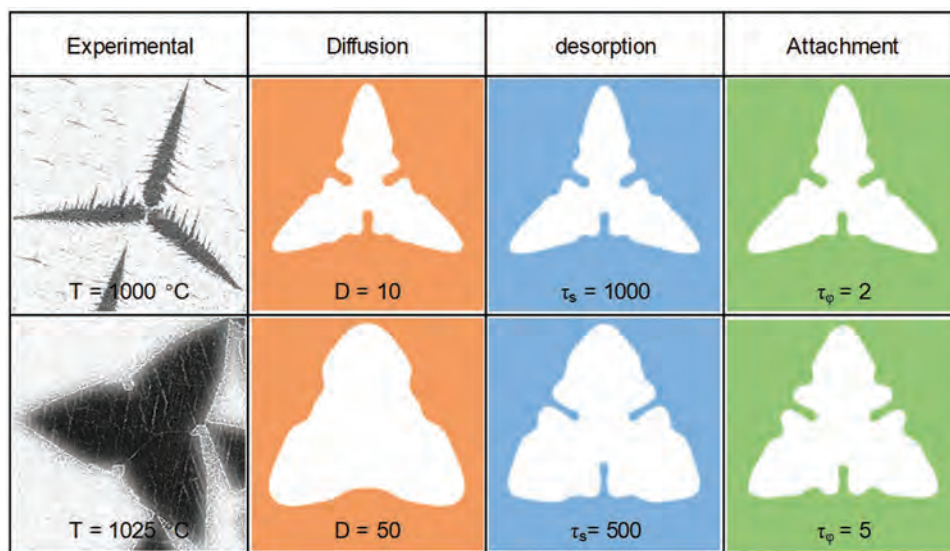
Figure 3. Phase-field simulation in comparison with experimental results. T, D, τ_s, and τ_ϕ are the growth temperature, diffusion coefficient, desorption time, and edge attachment time, respectively. The experimental SEM images display more spiny twigs grown at 1000 °C than that at 1025 °C. Diffusion simulation under $D = 10$ and 50 is obtained with $\tau_s = 1000$ and $\tau_\phi = 2$. Desorption simulation is obtained with $D = 10$ and $\tau_\phi = 2$. Attachment simulation is obtained with $D = 10$ and $\tau_s = 1000$.

on Cu substrate can be lowered from 0.95 to 0.9 eV, demonstrating the enhanced dehydrogenation.

Finally, large h-BN domains grown on Cu-Si alloy substrates are transferred to 300 nm oxide layer of silicon wafers. We observed the transferred samples under optical microscope. Most domains were monolayer, while triangular bilayer areas were found in the center of some domains. The lateral size of those bilayer triangles could reach tens of micrometers. We collected the Raman spectrum from mono- and bilayered h-BN region marked by the black and red dots in the inset of **Figure 4**a. The G band for monolayer and bilayer h-BN shifts from 1371 to 1367 cm^{-1}, consisting with previous work.[21] The Raman signal from the bare SiO$_2$/Si substrate is also collected for contrast, which shows the typical peak of third-order silicon transverse optic phonon at ≈1450 cm^{-1}. The Raman characterization here is not sufficient to give more crystallographic information due to the lack of detectable 2D band in h-BN few layers. However, taking advantage of the sensitivity to inversion symmetry breaking, SHG can easily reveal the crystalline information in BN few layers. The SHG mappings of a monolayer domain and a bilayer domain are shown in Figure 4b and Figure 4e, respectively. The incident laser is polarized in the direction highlighted by the arrows in the mappings and the SHG signal is collected in the same direction. The uniform SHG intensity from the whole domain confirms its single crystalline. We also plotted the intensity of SHG signals relative to the azimuth angle of the domains. For monolayer h-BN, the maximum SHG intensity should come from the orientation of crystal symmetry axis (armchair direction). All three armchair directions are identified from the polar image and the dashed line presents one of them (Figure 4c). Obviously, the symmetry of the h-BN triangular morphology is coincident with the crystalline orientation. Hence, we can utilize the triangular shape to identify the crystalline orientation. For the bilayer triangle in Figure 4e, its crystal symmetry could also be determined by its

shape orientation as confirmed by the polar image in Figure 4f. For bilayer h-BN, the SHG intensity is affected by not only the symmetric orientation but also the stacking sequence. AB stacking would lead to antiphase cancellation (destructive interference) of SHG from two adjacent layers, while AA' stacking enhances SHG due to constructive interference.[22] As shown in Figure 4e, the bilayer region exhibits much more intensive SHG than the monolayer region, indicating their same crystalline orientation. The SHG intensity is apparently enhanced by approximately four times due to the AA' stacking, which is consistent with the theory prediction.[23] However, for AB stacking in Figure 4d, the SHG signal from the second layer would destructively interfere with that from the first layer. The expected complete SHG cancellation does not occur probably because of the presence of strains in h-BN.

A small concentration of silicon can switch the CVD growth of h-BN on the Cu from the conventional attachment-limited regime to the diffusion-limited regime. Taking advantage of this strategy and the temperature dependence of diffusion, we realized delicate control of the morphology of h-BN domains, ranging from triangles and shuriken shape to fractal dendrites. Moreover, the doping of silicon can dramatically reduce the nucleation density and therefore provide a novel pathway for the large domain growth of h-BN.

Experimental Section

Preparation of Cu-Si Alloy Substrate: First, certain amounts of Si particles were mixed with ≈1 g Cu particles (99.99%) in a quartz crucible placing in an annealing furnace. The furnace chamber was pumped down to 0.1 Pa and hydrogen flow was introduced to maintain a 50 Pa pressure. Then, the Cu and Si particles were melted at 1080 °C for 10 min and annealed at 1035 °C for 1 h. After being cooled down, Cu-Si alloy beads were collected from the crucibles. Second, to obtain a flat growth surface, the Cu-Si beads were compressed to ≈1 mm thick discs.
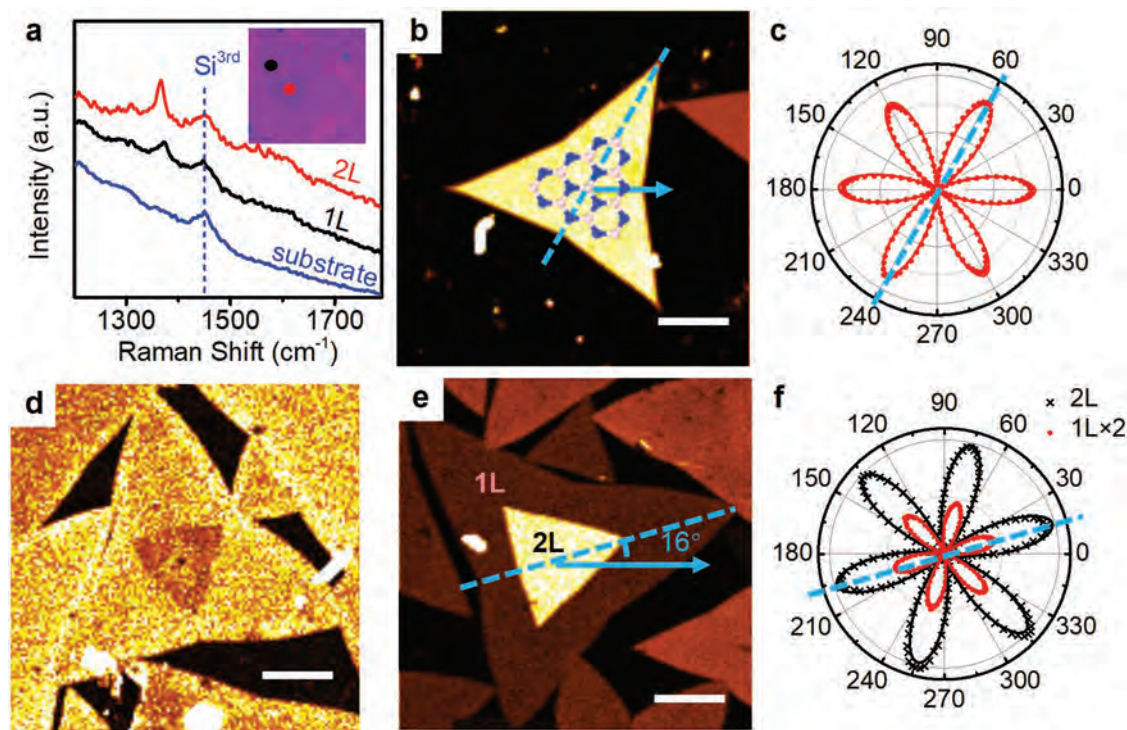
Figure 4. a) Raman spectra of the transferred h-BN domains, with the inset optical image marking the monolayer and bilayer by black and red dots. The blue dashed line locates the Raman peak from SiO_2/Si substrate. b,c) SHG mapping and the corresponding polarization pattern of a single layer h-BN domain. d) SHG mapping showing a large domain with an antiphase second layer at the center. e,f) SHG mapping and the corresponding polarization pattern of a large bilayer domain. The crystalline orientation of the second layer aligns with that of the first layer, leading to constructive interference of SHG signals. Scalar bars are 10 μm. Signal intensity from monolayer is doubled in panel (f) for better display.

Mechanically polishing with sandpaper and electrochemical polishing with 65% phosphoric acid solution were employed to reduce the surface roughness and remove the surface contaminants. Finally, other residues like silicon oxide particles were further removed from the surface via dipping the alloy disc into the hydrofluoric acid solution overnight. After that, the alloy disc was rinsed by deionized (DI) water for several times and dried by nitrogen gas flow.

Growth of h-BN Domains: First, the substrate was put inside a quartz tube of the CVD furnace. After the system was pumped down to 0.1 Pa, H2 flow was supplied. The H2 flow was adjusted to maintain a pressure of 50 Pa. Then, the furnace was heated up to 1030 °C and the sample was annealed for 1 h. Subsequently, the furnace was set to the target growth temperature, and the solid source, ammonia borane, was heated up, and maintained at 60–80 °C for 30–60 min for the CVD growth stage. Finally, the furnace was cooled down to room temperature naturally.

Transfer of h-BN Domains: Bubbling method was applied to transfer the h-BN domains. First, a polymethyl methacrylate (PMMA) layer was spin coated onto the substrate. Subsequently, the alloy sample was connected to the anode in 1 M NaOH solution, and another copper foil was used as the cathode. The current was increased until the surface of sample in the solution started to bubble. The PMMA film was peeled off from the surface as the sample was dipped down into the solution gradually. The PMMA film was rinsed by DI water for several times, which was then picked up by SiO_2/Si substrate and dried in air. The transferred sample was annealed at 150 °C, and the PMMA film was removed by acetone.

Material Characterization: The morphologies of h-BN domains were characterized by SEM (Zeiss, EVO 18) operating at 10 kV acceleration voltage. Raman spectroscopy (HORIBA, LabRAM HR Evolution) was conducted with a 532 nm continuous wave laser for h-BN analysis.

The SHG signals were excited by an 1100 nm femtosecond laser with a power density of ≈0.56 MW cm^{-2}.

Theory Calculations: The phase field model and first-principle calculations were described in the Supporting Information. For phase-field simulation, $n = 3$ was set, so a threefold symmetry was adopted. To simulate an anisotropic growth, $\varepsilon_g = 1/15$ and $\varepsilon_\tau = 1/1000$ were taken. Unless otherwise noted, $D = 10$, $\tau_s = 1000$, $F = 0.0005$, and $\tau_\phi = 2$ were taken. Each simulation started from a circle nucleus with a radius of 3 and ran on a square canvas.

Supporting Information

Supporting Information is available from the Wiley Online Library or from the author.

Acknowledgements

**ADVANCED
SCIENCE NEWS**

www.advancedsciencenews.com

**NANO · MICRO
small**

www.small-journal.com

Conflict of Interest

The authors declare no conflict of interest.

Keywords

[1] G. Cassabois, P. Valvin, B. Gil, *Nat. Photonics* **2016**, *10*, 262.

[2] Z. Liu, Y. Gong, W. Zhou, L. Ma, J. Yu, J. C. Idrobo, J. Jung, A. H. MacDonald, R. Vajtai, J. Lou, P. M. Ajayan, *Nat. Commun.* **2013**, *4*, 2541.

[3] a) C. R. Dean, A. F. Young, I. Meric, C. Lee, L. Wang, S. Sorgenfrei, K. Watanabe, T. Taniguchi, P. Kim, K. L. Shepard, J. Hone, *Nat. Nanotechnol.* **2010**, *5*, 722; b) B. Hunt, J. D. Sanchez-Yamagishi, A. F. Young, M. Yankowitz, B. J. LeRoy, K. Watanabe, T. Taniguchi, P. Moon, M. Koshino, P. Jarillo-Herrero, R. C. Ashoori, *Science* **2013**, *340*, 1427.

[4] a) Y. Kubota, K. Watanabe, O. Tsuda, T. Taniguchi, *Science* **2007**, *317*, 932; b) K. Watanabe, T. Taniguchi, H. Kanda, *Nat. Mater.* **2004**, *3*, 404.

[5] K. K. Kim, A. Hsu, X. Jia, S. M. Kim, Y. Shi, M. Hofmann, D. Nezich, J. F. Rodriguez-Nieva, M. Dresselhaus, T. Palacios, J. Kong, *Nano Lett.* **2012**, *12*, 161.

[6] a) Y. Hao, M. S. Bharathi, L. Wang, Y. Liu, H. Chen, S. Nie, X. Wang, H. Chou, C. Tan, B. Fallahazad, H. Ramanarayan, C. W. Magnuson, E. Tutuc, B. I. Yakobson, K. F. McCarty, Y.-W. Zhang, P. Kim, J. Hone, L. Colombo, R. S. Ruoff, *Science* **2013**, *342*, 720; b) T. Wu, X. Zhang, Q. Yuan, J. Xue, G. Lu, Z. Liu, H. Wang, H. Wang, F. Ding, Q. Yu, X. Xie, M. Jiang, *Nat. Mater.* **2016**, *15*, 43.

[7] X. Li, Y. Li, Q. Wang, J. Yin, J. Li, J. Yu, W. Guo, *Nano Res.* **2017**, *10*, 826.

[8] G. Lu, T. Wu, Q. Yuan, H. Wang, H. Wang, F. Ding, X. Xie, M. Jiang, *Nat. Commun.* **2015**, *6*, 6160.

[9] S. Caneva, R. S. Weatherup, B. C. Bayer, B. Brennan, S. J. Spencer, K. Mingard, A. Cabrero-Vilatela, C. Baehtz, A. J. Pollard, S. Hofmann, *Nano Lett.* **2015**, *15*, 1867.

[10] J. Meng, X. Zhang, Y. Wang, Z. Yin, H. Liu, J. Xia, H. Wang, J. You, P. Jin, D. Wang, X. Meng, *Small* **2017**, *13*, 1604179.

[11] Y. Ji, B. Calderon, Y. Han, P. Cueva, N. R. Jungwirth, H. A. Alsalman, J. Hwang, G. D. Fuchs, D. A. Muller, M. G. Spencer, *ACS Nano* **2017**, *11*, 12057.

[12] a) J. Yin, J. Yu, X. Li, J. Li, J. Zhou, Z. Zhang, W. Guo, *Small* **2015**, *11*, 4497; b) C. Jin, F. Lin, K. Suenaga, S. Iijima, *Phys. Rev. Lett.* **2009**, *102*, 195505.

[13] a) Y. Stehle, H. M. Meyer, R. R. Unocic, M. Kidder, G. Polizos, P. G. Datskos, R. Jackson, S. N. Smirnov, I. V. Vlassiouk, *Chem. Mater.* **2015**, *27*, 8041; b) Z. Zhang, Y. Liu, Y. Yang, B. I. Yakobson, *Nano Lett.* **2016**, *16*, 1398.

[14] X. Yan, Y. A. Chang, *J. Alloys Compd.* **2000**, *308*, 221.

[15] J. Li, Y. Li, J. Yin, X. Ren, X. Liu, C. Jin, W. Guo, *Small* **2016**, *12*, 3645.

[16] a) V. Babenko, G. Lane, A. A. Koos, A. T. Murdock, K. So, J. Britton, S. S. Meysami, J. Moffat, N. Grobert, *Sci. Rep.* **2017**, *7*, 14297; b) X. Wang, T. N. Hooper, A. Kumar, I. K. Priest, Y. Sheng, T. O. M. Samuels, S. Wang, A. W. Robertson, M. Pacios, H. Bhaskaran, A. S. Weller, J. H. Warner, *CrystEngComm* **2017**, *19*, 285.

[17] a) Y. Liu, S. Bhowmick, B. I. Yakobson, *Nano Lett.* **2011**, *11*, 3113; b) E. Ćavar, R. Westerström, A. Mikkelsen, E. Lundgren, A. S. Vinogradov, M. L. Ng, A. B. Preobrajenski, A. A. Zakharov, N. Mårtensson, *Surf. Sci.* **2008**, *602*, 1722; c) Y. Shi, C. Hamsen, X. Jia, K. K. Kim, A. Reina, M. Hofmann, A. L. Hsu, K. Zhang, H. Li, Z.-Y. Juang, M. S. Dresselhaus, L.-J Li, J. Kong, *Nano Lett.* **2010**, *10*, 4134.

[18] W. W. Mullins, R. F. Sekerka, *J. Appl. Phys.* **1964**, *35*, 444.

[19] a) A. Karma, M. Plapp, *Phys. Rev. Lett.* **1998**, *81*, 4444; b) A. Karma, W. J. Rappel, *Phys. Rev. E* **1996**, *53*, R3017; c) J. B. Collins, H. Levine, *Phys. Rev. B* **1985**, *31*, 6119.

[20] B. M. Srinivasan, Y. Hao, R. Hariharaputran, S. Rywkin, J. C. Hone, L. Colombo, R. S. Ruoff, Y.-W. Zhang, *ACS Nano* **2018**, *12*, 9372.

[21] Q. Cai, D. Scullion, A. Falin, K. Watanabe, T. Taniguchi, Y. Chen, E. J. G. Santos, L. H. Li, *Nanoscale* **2017**, *9*, 3059.

[22] a) C.-J. Kim, L. Brown, M. W. Graham, R. Hovden, R. W. Havener, P. L. McEuen, D. A. Muller, J. Park, *Nano Lett.* **2013**, *13*, 5660; b) T. Jiang, H. Liu, D. Huang, S. Zhang, Y. Li, X. Gong, Y.-R. Shen, W.-T. Liu, S. Wu, *Nat. Nanotechnol.* **2014**, *9*, 825; c) X. Zhou, J. Cheng, Y. Zhou, T. Cao, H. Hong, Z. Liao, S. Wu, H. Peng, K. Liu, D. Yu, *J. Am. Chem. Soc.* **2015**, *137*, 7994.

[23] a) Y. Li, Y. Rao, K. F. Mak, Y. You, S. Wang, C. R. Dean, T. F. Heinz, *Nano Lett.* **2013**, *13*, 3329; b) W.-T. Hsu, Z.-A. Zhao, L.-J. Li, C.-H. Chen, M.-H. Chiu, P.-S. Chang, Y.-C. Chou, W.-H. Chang, *ACS Nano* **2014**, *8*, 2951.